

In Situ Optimization of an Optoelectronic Reservoir Computer with Digital Delayed Feedback

Fyodor Morozko Shadad Watad Amir Naser Andrey Novitsky Alina Karabchevsky*

F. Morozko, S. Watad, A. Naser, A. Karabchevsky¹

School of Electrical and Computer Engineering

Ben-Gurion University of the Negev

Beer-Sheva 8410501, Israel

E-mail: alinak@bgu.ac.il

A. Novitsky

Belarusian State University

Minsk, 220030, Belarus

A. Karabchevsky²

Department of Physics

Lancaster University

LA1 4YB, United Kingdom

Keywords: *reservoir computing, neuromorphic computing, physical computing, optoelectronic oscillator, in situ optimization*

Reservoir computing (RC) is an innovative paradigm in neuromorphic computing that leverages fixed, randomized, internal connections to address the challenge of overfitting. RC has shown remarkable effectiveness in signal processing and pattern recognition tasks, making it well-suited for hardware implementations across various physical substrates, which promise enhanced computation speeds and reduced energy consumption. However, achieving optimal performance in RC systems requires effective parameter optimization. Traditionally, this optimization has relied on software modeling, limiting the practicality of physical computing approaches. Here, we report an *in situ* optimization method for an optoelectronic delay-based RC system with digital delayed feedback. By simultaneously optimizing five parameters, normalized mean squared error (NMSE) of 0.028, 0.561, and 0.271 is achieved in three benchmark tasks: waveform classification, time series prediction, and speech recognition outperforming simulation-based optimization (NMSE 0.054, 0.543, and 0.329, respectively) in the two of the three tasks. This method marks a significant advancement in physical computing, facilitating the optimization of RC and neuromorphic systems without the need for simulation, thus enhancing their practical applicability.

1 Introduction

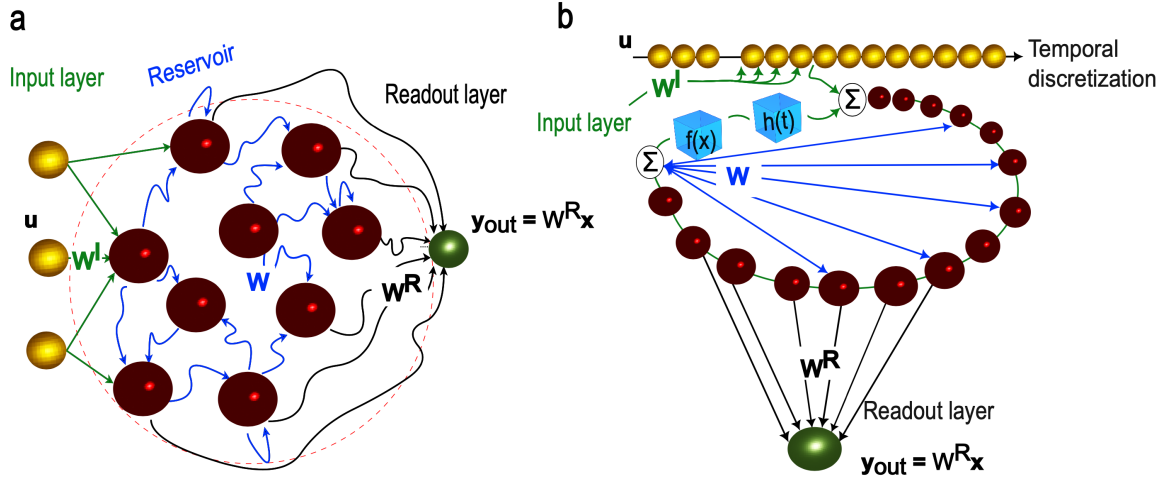
Artificial Neural Networks (ANNs) are powerful machine learning algorithms modeled after biological neural systems, consisting of interconnected neurons arranged in layers. This architecture allows ANNs to perform exceptionally well in tasks such as pattern recognition and decision-making [1]. Over the past decade, the rapid development of GPU-accelerated Deep Neural Networks (DNNs) with multiple layers has significantly expanded the use and application of these models [2].

However, deep models' increasing complexity and size have led to high energy consumption during training. Additionally, while ANNs are inherently analog, their implementation within traditional von Neumann-Turing architectures incurs significant computational overhead regarding speed and energy efficiency. As the demand for more powerful ANNs grows and the limitations of Moore's law become more pronounced, there is a critical need to explore analog or physical computing alternatives to address these challenges.

Optical neuromorphic computing has emerged as a promising solution for improving data processing, offering advantages such as parallelism, high bandwidth, low noise, and reduced energy consumption [3, 4, 5, 6, 7, 8, 9, 10, 11].

In this context, reservoir computing (RC) presents an effective approach by utilizing fixed, randomized internal connections to reduce the computational complexity of training and mitigate overfitting [12, 13, 14]. RC consists of a network of nonlinear nodes randomly interconnected with weights W . This reservoir network receives data to be processed via the input layer characterized by input weights W^I . The input signal causes transient responses in the reservoir nodes, which are submitted to the readout layer

and are linearly weighted to form the readout signal. The training of RC comprises a linear regression problem to find the optimal readout weights W^R . The idea of RC is to perform a nonlinear mapping of the input data onto higher-dimensional space in which distinct data classes can be linearly separated [15, 16, 17]. Schematics shown in **Figure 1a** illustrates the principle of RC.



10

Figure 1: **a** Generic reservoir computing principle. The depicted layout consists of distinct components: an input layer (bronze spheres) responsible for receiving external data, a reservoir (ruby spheres) featuring randomized fixed connections, and a linear readout layer (green spheres). **b** Delay reservoir computing. $f(x)$ is the activation function performing the nonlinear transformation exhibited by the element, and $h(t)$ is the impulse response. W , W^I and W^R are, respectively, reservoir, input, and readout connectivity matrices.

It was suggested to implement an RC network in a system consisting of a single node subject to delayed feedback [15]. In delay RC the nodes are distributed along the delay line while the input data is injected in time-multiplexed form as shown in Figure 1b. Such an approach offers significant simplification of physical implementation compared to traditional RC. Owing to this simplicity delay RC systems became among the first implementations of optical neuromorphic computing and have shown exceptional performance in signal processing and pattern recognition [18, 19, 20, 21, 22, 23, 24].

Despite the relative simplicity of training, reservoir computing (RC) demands a careful selection of architectural parameters, known as hyperparameters, including reservoir size, nonlinearity strength, and input scaling [25, 26]. The complexity of hyperparameter optimization increases exponentially with the number of parameters, leading to a substantial computational burden when designing physical computing systems that typically rely on simulations in conventional hardware. This reliance obscures the inherent advantages of physical computing. This aspect is often overlooked in the physical computing literature, where the focus is on hardware implementations rather than the optimization process.

Here, we address the challenge of optimizing an optoelectronic delay-based reservoir computing (RC) system through an *in situ* approach. We optimize five key hyperparameters simultaneously: the delay-to-clock cycle ratio, input scaling, phase bias, nonlinearity gain, and the regularization parameter used in readout training. The effectiveness of this *in situ* optimization is demonstrated across three benchmark tasks: classification of sinusoidal versus rectangular waveforms, NARMA10 time-series prediction, and Japanese vowel classification. Our method achieves state-of-the-art normalized mean squared error (NMSE) values of 0.028, 0.561, and 0.271, respectively.

Furthermore, we experimentally validate theoretical predictions from Refs. [27, 28] which were never realized, and show that resonances between the delay and clock cycle timescales adversely affect RC accuracy, particularly in the NARMA10 task. This is evidenced by significant variations in NMSE, ranging from 0.561 to over 1, depending on the delay-to-clock cycle ratio. These findings provide valuable insights into optimizing the performance of delay-based RC systems for various computational tasks.

2 Theoretical Background

2.1 Principle of Reservoir Computing

The evolution of the reservoir characterized by a state vector \mathbf{x} driven by a data signal \mathbf{u} can be described as [13, 15]

$$\mathbf{x}(n+1) = f(\beta W \mathbf{x}(n) + \rho W^I \mathbf{u}(n+1)), \quad (1)$$

where β and ρ are the feedback and input scaling, respectively, n is the discrete time, f is a nonlinear activation function, and W , W^I are the reservoir and input connectivity matrices, respectively. The reservoir's transient response to the input signal is sent to a linear read-out layer where it is weighted by the readout matrix W^R to obtain the output vector \mathbf{y}_{out} as

$$\mathbf{y}_{\text{out}}(n) = W^R \mathbf{x}(n). \quad (2)$$

Training of the reservoir is typically performed by finding the weights (elements of matrix W^R) minimizing the mean squared error (MSE) between the target output \mathbf{y}_t and reservoir's readout given by Eq. (2) $\|\mathbf{y}_t - W^R \mathbf{x}\|^2$ on a training dataset using linear regression. To avoid overfitting, it is expected to minimize $\|\mathbf{y}_t - W^R \mathbf{x}\|^2 + \|\lambda W^R \mathbf{x}\|^2$, where the second term stands for weights regularization with the regularization constant λ also referred to as ridge constant. Due to the linearity of the readout layer, it is possible to find the readout weights by simple matrix inversion as

$$W^R = Y X^T (X X^T + \lambda I)^{-1}, \quad (3)$$

where X and Y are matrices obtained by column-wise concatenation of all reservoir states $\mathbf{x}(n)$ with $n = 0, 1, \dots, N-1$ and all target outputs $\mathbf{y}_t(n)$ with $n = 0, 1, \dots, N-1$, respectively, where I is the identity matrix [29]. The performance of the reservoir is evaluated by measuring the error on a validation dataset not seen during training. One of the commonly used error metrics for evaluation is the normalized mean squared error (NMSE) defined as

$$\text{NMSE} = \frac{\|\mathbf{y} - \hat{\mathbf{y}}\|^2}{\sigma_{\mathbf{y}}^2}, \quad (4)$$

where \mathbf{y} and $\hat{\mathbf{y}}$ are the target and the actual response on the validation dataset, respectively, while $\sigma_{\mathbf{y}}^2$ is the variance of the target response [30]. A related metric is the normalized root mean square error (NRMSE) which is the square root of NMSE.

2.2 Delay-Based Reservoir Computing

To relate temporal dynamics of a delay-based reservoir with the evolution equation (1) the values of the state variable $x(t)$ sampled at evenly spaced instants of time during a clock cycle period T are mapped via time multiplexing to the components of the reservoir's state vector $\mathbf{x}(n) \equiv x^i(n)$ forming a set of virtual neurons as shown in Figure 1b

$$\mathbf{x}(n) \equiv x^i(n) = x(i\theta + nT), \quad (5)$$

where $i = 0, \dots, k-1$, $\theta = T/k$ is the virtual neurons temporal separation with k being the size of the reservoir. To map the input signal onto the virtual nodes of the reservoir, input masking is performed by applying sample-and-hold operation onto the input and multiplying by a periodic piecewise-constant function with the period T [15, 31]. For establishing interactions between different neurons in successive layers (expressed by off-diagonal entries in the matrix W of Eq. (1)) several approaches to time multiplexing exist: in [19] delay and clock cycle were synchronous $\tau = T$ while an introduced low-pass transient characteristic caused neighboring neurons to interact, in [21], analogously, delay and clock cycle were synchronized, but multiple fractional delays were introduced. It was observed by Rodan *et al.* [32] and first exploited in hardware by Paquot *et al.* [18] that desynchronization of the clock cycle and delay time leads to a more interconnected reservoir topology by causing different neurons in the successive

recurrent layers to interact. Specifically, in [18, 23] delay time was set to $\tau = T + \theta$ providing minimum complexity network structure suggested in [32]. The structure of a delay-based RC is schematically shown in Figure 1b.

2.3 Reservoir Computing in Optoelectronic Oscillator

An example of a delay system in photonics is an optoelectronic oscillator, a system consisting of a laser light source, electro-optic modulator, a photodetector whose output is connected to the modulation port of the modulator forming a closed loop. Sinusoidal transmission characteristic of a Mach-Zehnder electro-optic modulator renders the system nonlinear while introducing a delay into the feedback loop leads to the emergence of multiple-valued stationary states, causing the system to exhibit complex nonlinear behavior [33, 34]. Particularly, optoelectronic oscillator, upon the tuning of laser power, photodetector gain, and phase bias of the modulator, can exhibit transitions between stable, multi-stable, periodic, and chaotic dynamics known as Hopf bifurcations [35, 36, 37].

Dynamics of an optoelectronic oscillator can be described by Ikeda model [33, 34, 36, 37] according to which voltage V at the modulation port of MZM follows the delay-differential equation

$$V(t) + T_R \frac{dV}{dt}(t) = G^* P[V(t - \tau)], \quad (6)$$

where $P[V]$ is the power transmitted by the MZM and received by the photodetector, τ is the delay time, G^* is the voltage gain of the photodetector, and, T_R is the response time of the system. The transmission characteristic $P[V]$ of the Mach-Zehnder modulator is given by [35, 36, 37]

$$P[V] = \frac{1}{2} P_{\max} (1 + M \sin(\pi(V + V_B)/V_\pi + \phi)), \quad (7)$$

where P_{\max} is the total optical power in the system, M , V_π , and ϕ are the modulation depth, half-wave voltage, and intrinsic phase of the MZM, respectively, and V_B is the bias voltage at the bias port of the MZM. If the response time is much shorter than the delay time $T_R \ll \tau$, the derivative in Eq. (6) can be neglected, and we can describe the dynamics $V(t)$ by a difference equation [35]

$$V(t) = G^* P[V(t - \tau)], \quad (8)$$

while analyzing $V(t)$ at discrete time steps $t = t_0 + n\tau$. Introducing the dimensionless state variable $x = V/V_\pi$, performing time multiplexing according to **Eq. (5)**, and adding external signal we rewrite Eq. 8 in terms of a generic RC evolution Eq. (1) as

$$\mathbf{x}(n+1) = \frac{G}{2} (1 + M \sin(\beta W \mathbf{x}(n) + \rho W^I \mathbf{u}(n+1) + \Phi_0)), \quad (9)$$

where $\Phi_0 = \phi + \pi V_B/V_\pi$ is the phase bias, β and ρ are the feedback and input scaling, respectively, and $G = G^*/V_\pi P_{\max}$ is the net gain. In delay RC the matrix W is generally a circulant matrix whose entries depend on the ratio of the delay time τ to the clock cycle T while the matrix W^I is initialized with uniformly distributed entries in the $[-1, 1]$ interval.

3 Experimental setup

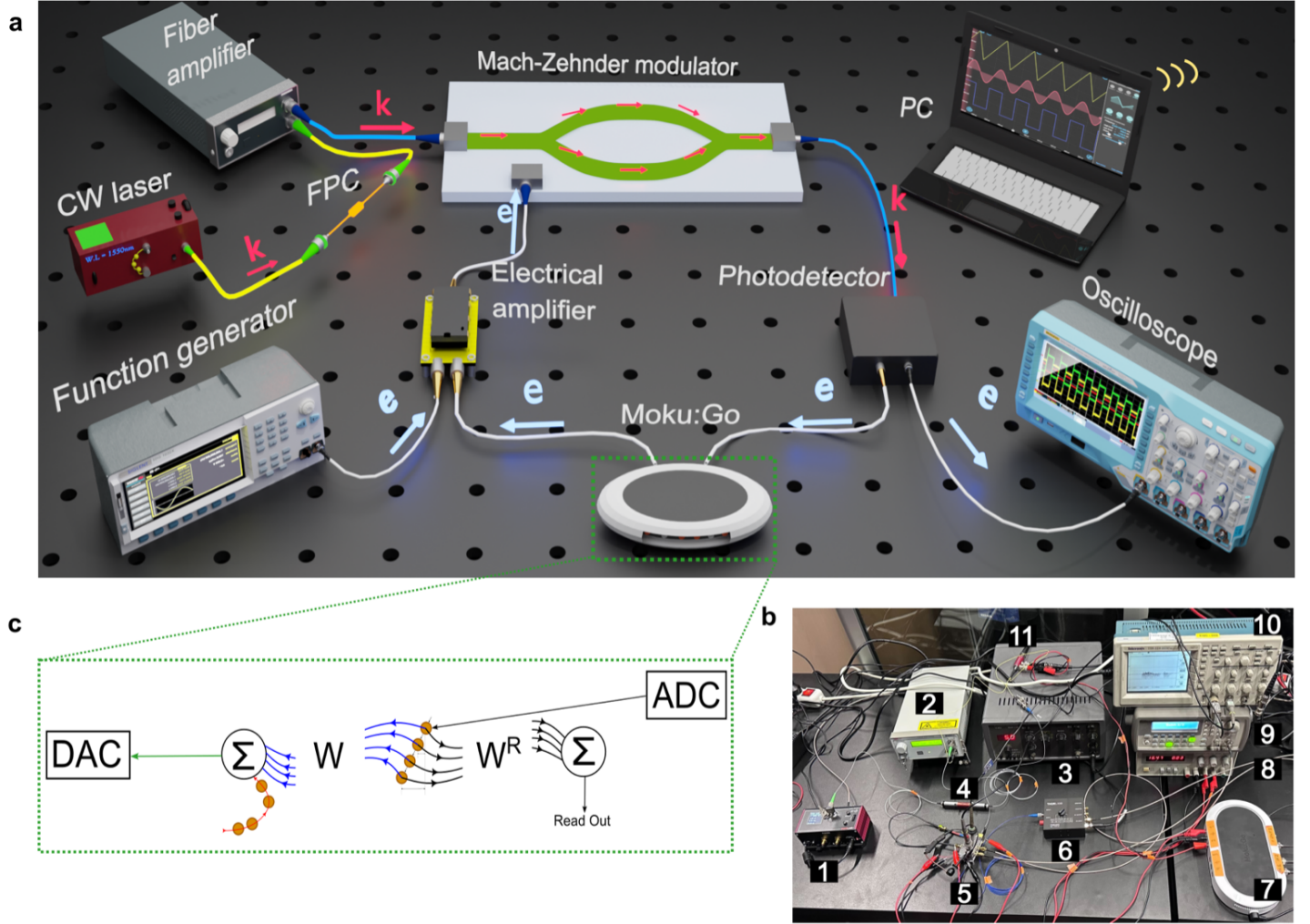


Figure 2: **a.** An artistic impression of the experimental set-up. A continuous wave (CW) laser beam is directed into the fiber polarization controller (FPC), which aligns the light polarization with the slow axis of the modulator. Subsequently, the laser beam is coupled to a fiber amplifier to maintain the system's stability. This amplified laser light is modulated with a Mach-Zehnder modulator (MZM), whose sinusoidal transmission function introduces nonlinearity into the reservoir. The modulated light is detected by a photodetector, delayed with Moku:Go's FPGA-based delay, amplified, and sent to the modulation input of the MZM, forming a closed loop. The external signal is mixed with the delayed feedback. Note: the components are out of scale for visualization. **b.** Photograph of the experimental setup, components are labeled as follows: 1. continuous-wave (CW) laser, 2. Erbium-doped fiber amplifier (EDFA), 3. function generator producing trigger signal, 4. fiber polarization controller (FPC), 5. Mach-Zehnder modulator (MZM) with electrical driver, 6. photodetector, 7. Moku:Go, 8. power supply for the electrical driver, 9. arbitrary waveform generator (AWG), 10. oscilloscope, 11. variable optical attenuator (VOA). **c.** Schematics of the digital delay and data digitizer implemented in the Moku:Go component: delayed feedback implements the reservoir's connectivity matrix W while the digitized reservoir states are weighted with the readout matrix W^R .

The experimental setup is illustrated in **Figure 2a**, which provides an artistic rendering of the system. Additionally, Figure 2b presents a photograph of the actual physical system implemented in the laboratory. We have used a continuous-wave (CW) laser at a wavelength of 1550 nm (KLS1550, Thorlabs) as a monochromatic light source. The laser was connected through a fiber polarization controller (PC1100, Fiberpro) to an Erbium-doped fiber amplifier (EDFA) (EDFA100S, Thorlabs) operated in a saturated regime. The EDFA was used to increase the maximum optical power level, while the variable optical attenuator (VOA) was used to adjust the optical power level in the reservoir. The attenuated optical signal was modulated with a Mach-Zehnder modulator (MZM) (LN81S-FC, Thorlabs) produced in X-cut lithium niobate. The modulated optical signal was detected and amplified with an InGaAs photodetector (PDB450C, Thorlabs) with an embedded switchable gain trans-impedance amplifier. The photodetector's voltage output was sent to Moku:Go (Liquid Instruments), an FPGA-based instrument that implements delay lines and data acquisition. We note that the delayed feedback introduces the system's short-time memory property, while the MZM's sinusoidal transmission characteristic creates nonlinearity. Moku:Go was also used as a voltage source controlling the phase bias of the MZM and attenuation of the VOA. The output of Moku:Go was mixed with the input signal synthesized with an arbitrary waveform generator (33220A, Agilent). The mixed signal was amplified with a driver circuit based on an operational amplifier (LM7171, Texas Instruments) to drive the MZM.

Delayed feedback tuning using FPGA Delayed feedback was implemented using an FPGA operating as the finite impulse response (FIR) filter

$$\tilde{x}(t) = \sum_{l=0}^{L-1} h_l x(t - l/r), \quad (10)$$

where $x(t)$ and $\tilde{x}(t)$ are the input and the output of the FIR filter, respectively, h_l are the filter tap coefficients, L is the filter order, and r is its sampling rate. In the experiment all FIR filter coefficients but the last were set to zero while the last coefficient was set to 1, ensuring the delay time $\tau = (L - 1)/r$. FPGA operated at either sampling rate $r=3.906$ MHz or $r=976.6$ kHz. The filter order L was varied in the range $L \in [2, 232]$ at $r=3.906$ MHz and in the range $L \in [2, 464]$ at $r=976.6$ kHz. By varying FIR filter order L we tuned the delay time in the range $[0.5, 60]$ and $[2, 475]$ μs at the sampling rate 3.906 MHz and 976.6 kHz, respectively.

Data injection and acquisition Reservoir transient responses were digitized using the Moku:Go's built-in datalogger operating at a sampling rate of $f = 488.3$ kHz equal to the $1/8$ or $1/2$ of the sampling rate of the delayed feedback. The time separation θ between the virtual neurons was set to $1/f$ so that each neuron corresponded to one sample in the data log. The readout training was performed in software using routines from the reservoirpy library [29]. To synchronize the reservoir's readout with the input signal, we employed an external function generator (label 3 in Figure 2b), producing a trigger signal that triggered bursts on the AWG and started data acquisition on the Moku:Go's datalogger. Individual inputs were concatenated in batches to speed-up the reservoir optimization so that waveforms filled all the available AWG's memory.

4 Results

In this section, we present the results of *in situ* optimization of our experimental RC system in three benchmark tasks and compare them to the simulation. In each task we simultaneously optimized five parameters: gain G , phase bias Φ_0 , input scaling ρ , delay time τ , and regularization parameter λ . For the optimization, a Bayesian algorithm was employed [38, 29, 26] along with random search.

Sinusoidal versus rectangular waveform classification As a first experiment, we have trained the reservoir to distinguish sinusoidal from rectangular waveforms following Paquot *et al.* [18]. Departing from

the Ref. [18] we varied the frequency of the waveforms to increase complexity of the task. For the training, the dataset consisting of a total of 20 waveforms was split equally into train and test sets. **Figure 3** presents the simulated and experimental reservoir performance on the test dataset. As the figure shows, simulated and experimental reservoirs were capable of classifying waveforms nearly perfectly. The experimental system, however, exhibited a slightly more stable readout signal, resulting in NMSE outperforming simulation by almost a factor of 2: 0.028 and 0.054, respectively.

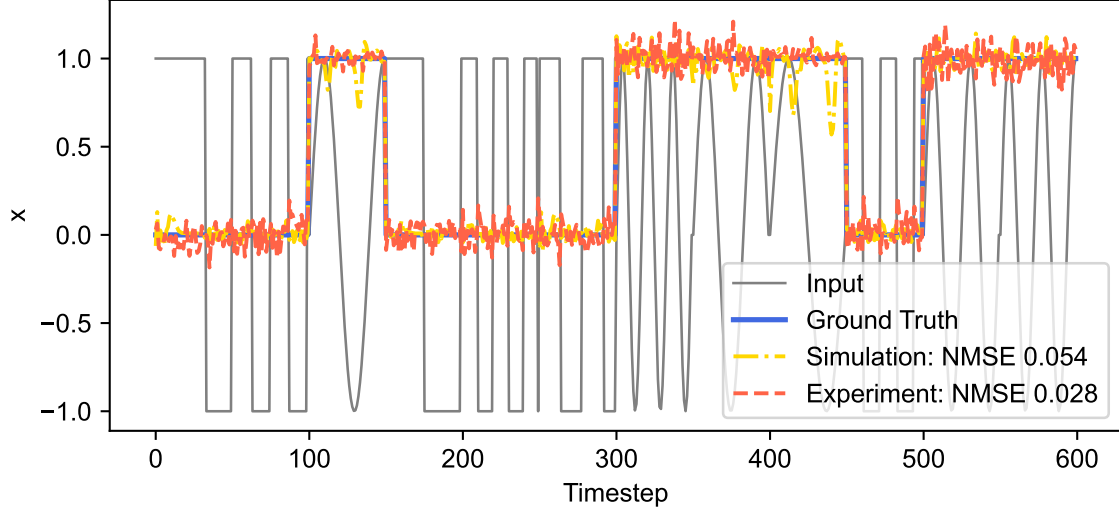


Figure 3: Sinusoidal vs. rectangular waveform classification task. The solid grey curve represents the input signal (sinusoidal and rectangular waveforms), a solid blue curve represents the target response ($x=1$ for sinusoidal, $x=0$ for rectangular waveform), the dash-dotted yellow and orange dashed curves represent the readout of simulated and *in situ*-optimized experimental reservoirs, respectively. Experimental reservoir settings: input scaling $\rho=0.19$, net gain $G=0.39$, phase bias $\Phi_0=0.67\pi$, delay $\tau=0.27T$, regularization parameter $\lambda = 1.4 \times 10^{-3}$.

The optimal parameter settings obtained *in situ* were: input scaling $\rho=0.19$, net gain $G=0.39$, phase bias $\Phi_0=0.67\pi$, delay $\tau=0.27T$, and regularization $\lambda = 1.4 \times 10^{-3}$.

NARMA10 time series recovery For a second benchmark we trained reservoir to predict time series generated by the Nonlinear Auto Regressive Moving Average (NARMA) model [32, 18], a popular benchmark task in the RC literature.

We used a NARMA model of the order ten driven by the equation

$$y(n+1) = 0.3y(n) + 0.05y(n) \left(\sum_{i=0}^9 y(n-i) \right) + 1.5u(n-9)u(n) + 0.1, \quad (11)$$

analogous to the model in Refs. [32, 18] and [28].

The total length of the dataset was 8000 steps; the dataset was randomly split into train and test sets 4000 steps length each.

Reservoir performance in this task is presented in **Figure 4**. One observes almost identical behavior of simulated and experimental reservoirs and similar NMSE of 0.543 vs. 0.561, respectively.

The optimal settings of the reservoir were found to be $\rho=0.33$, $G = 0.7$, $\Phi_0 = 0.68\pi$, $\tau = 0.49T$, and $\lambda = 5 \times 10^{-3}$ for the reservoir of size 50. The best reservoir configuration for this task performed 0.534 and 0.731 in terms of NMSE and NRMSE, respectively, at a reservoir size of 50.

NMSE in our case is considerably higher than the in Ref. [18] (0.168) but is within the range of NMSEs reported in Ref. [28] (0.04-0.64) for simulated delay reservoirs of the same size. We attribute increased NMSE in our case to the larger dataset size compared to Ref. [18] (8000 vs 2000 timesteps).

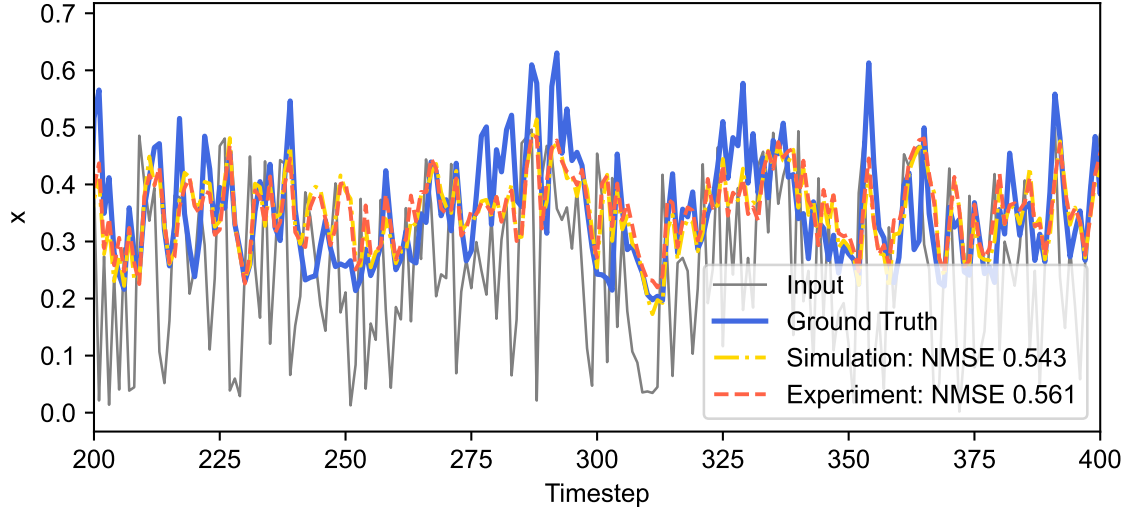


Figure 4: NARMA10 time series recovery. The solid grey curve represents the input signal (white noise), the solid blue curve represents the time series governed by the NARMA10 model (Eq. (11)), the dash-dotted yellow and dashed orange curves represent the readout of simulated and *in situ*-optimized reservoirs, respectively. Experimental reservoir settings: input scaling $\rho=0.33$, net gain $G=0.7$, phase bias $\Phi_0=0.68\pi$, delay $\tau=0.49T$, regularization parameter $\lambda=5 \times 10^{-3}$.

Japanese vowels classification. To assess the speech recognition capability of our system, we tested it on the Japanese Vowels dataset [39]. This dataset contains a 640-time series of 12 Mel-frequency cepstrum coefficients (MFCCs) taken from recordings of nine speakers uttering a Japanese vowel. The task is to classify the recordings by the speaker's identity.

Figure 5 shows the multiplexed waveforms of input data (a), target output (ground truth) (b), simulated and experimental reservoirs' readout (c-d).

In this task, *in situ*-optimized reservoir outperformed simulation in terms of NMSE by about 17% (0.271 vs 0.329) demonstrating almost identical word error rate (WER) of 6.5% vs. 6.4%. Our result is comparable to the 5% WER in Ref. [40] for the reservoir of size 50 and outperforms the result in [41] with 18.5% WER.

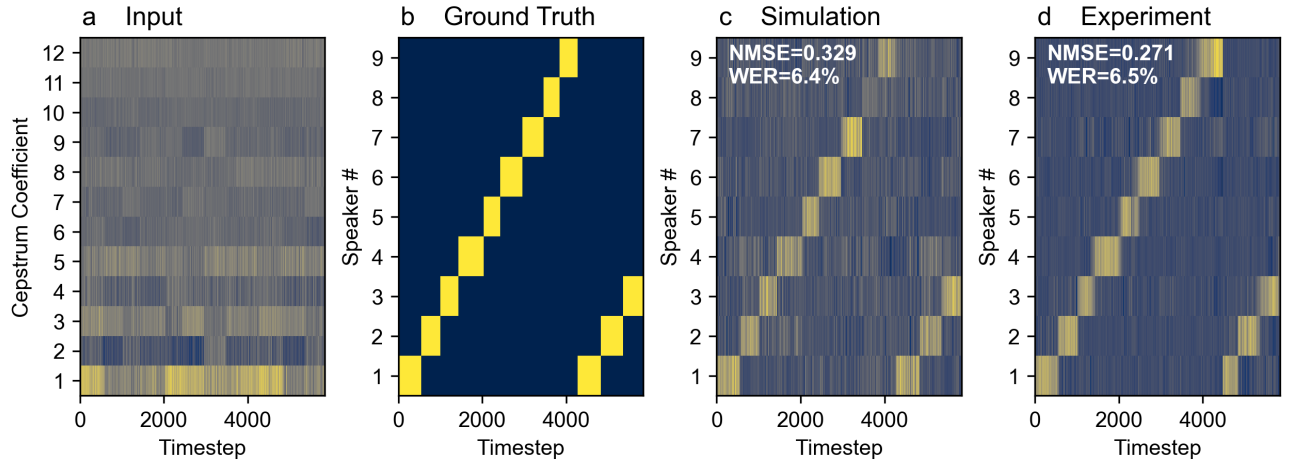


Figure 5: Japanese vowels classification task. Multiplexed waveforms of **a.** input data, **b.** ground truth, **c-d** simulated and experimental reservoirs' readouts. Reservoir settings: input scaling $\rho=0.47$, net gain $G=0.52$, phase bias $\Phi_0=0.44\pi$, delay $\tau=0.35T$, regularization parameter $\lambda=3 \times 10^{-7}$.

The optimal settings of the reservoir were found to be: $\rho=0.47$, $G=0.52$, $\Phi_0=0.44\pi$, $\tau=0.35T$, and $\lambda=3 \times 10^{-7}$ for the reservoir with 50 nodes.

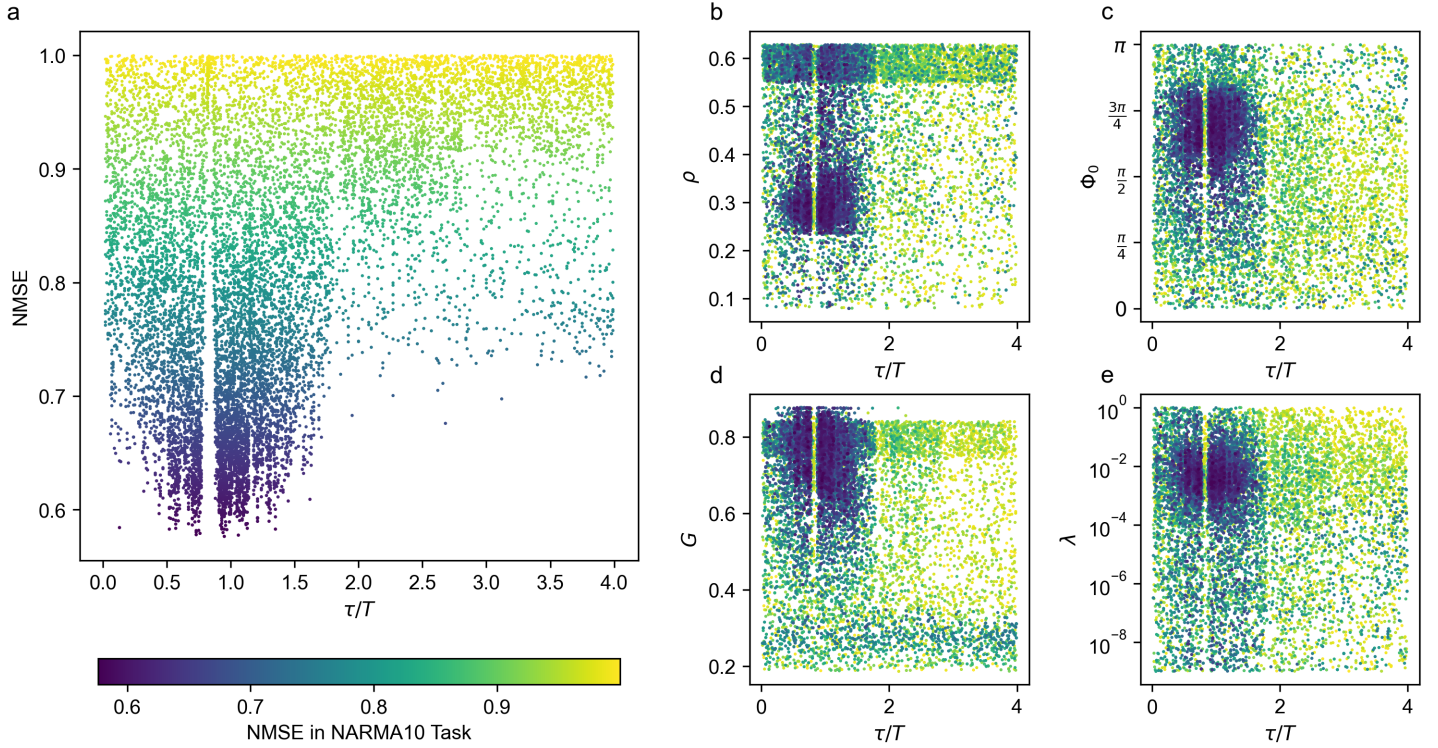


Figure 6: *In situ* optimization results. Normalized mean square error (NMSE) in NARMA10 task as a function of **a.** delay to clock cycle ratio τ/T and **b-e** τ/T together with another parameter of the reservoir: **b.** τ/T and input scaling ρ , **c.** τ/T and phase bias Φ_0 , **d.** τ/T and net gain G , **e.** τ/T and regularization parameter λ . Each point in the plots corresponds to a tested reservoir parameter setting.

Effect of the parameters on the RC accuracy To illustrate the performance dependence of the system on its parameters **Figure 6** shows the results of optimization for the NARMA10 task.

We learn that for input scaling ρ , phase bias Φ_0 , and regularization parameter λ within the studied range, there is a single local optimum centered at $\rho \approx 0.3$, $\Phi_0 \approx 3\pi/4$, and $\lambda \approx 10^{-3}$, respectively. The picture for G is more interesting: one can observe a wide local optimum above $G \approx 0.6$ spanning to the top boundary and an additional local optimum near $G = 0.3$. Regarding the delay-to-clock cycle ratio, multiple narrow peaks and drops in NMSE are seen with the best performance within the range $\tau/T \in [0, 2]$. The most prominent peak corresponds to the primary resonance $\tau/T \approx 1$ but is shifted to the left due to the latency of FPGA, resulting in underestimated τ . Noteworthy, the performance peaks and drops at specific τ/T ratios are independent of other parameters of the reservoir, confirming that the root cause for the detrimental effect on the performance are delay to clock cycle resonances that lead to the reduction of RC network complexity, as discussed in Refs. [42, 27, 28].

5 Conclusion

In this work, we have achieved *in situ* optimization of a physical computing system based on the optoelectronic delay reservoir computing principle. We showed that by evaluating the system across three benchmark tasks—signal classification, time series prediction, and speech recognition—we demonstrated that *in situ* optimization significantly enhances accuracy, with improvements of 17% and 48% in two of the tasks compared to conventional simulation-based approaches. Beyond improving accuracy, *in situ* optimization leverages the inherent speed and energy efficiency of physical computing systems while also eliminating the need for extensive numerical modeling, which often requires accounting for noise, environmental factors, and device-specific characterization.

In conclusion, reservoir computing (RC) is a powerful approach in neuromorphic computing that uses fixed, randomized internal connections to mitigate overfitting, making it highly effective for signal pro-

cessing and pattern recognition tasks. Its suitability for hardware implementations across various physical platforms offers significant potential for increased computational speed and reduced energy consumption. However, achieving optimal performance in RC systems has traditionally required software-based optimization, limiting the practicality of physical computing solutions.

In this work, we introduced an *in situ* optimization method for an optoelectronic delay-based RC system with digital delayed feedback. By simultaneously optimizing five key parameters, we achieved normalized mean squared error (NMSE) values of 0.028, 0.561, and 0.271 in three benchmark tasks—waveform classification, time series prediction, and speech recognition—outperforming simulation-based optimization in two of these tasks.

This *in situ* optimization method represents a significant advancement in physical computing, eliminating the need for extensive simulations and enhancing the practical applicability of RC and neuromorphic systems across real-world applications.

Overall, this study demonstrates the potential of *in situ* optimization to advance the efficiency and performance of physical computing systems, offering a promising pathway for more effective implementations in real-world applications.

Acknowledgements

The research was supported by the EU ERA-NET DIEGO project Ministry of Energy, Grant No. 221-11-032, and the Lower Saxony's Minister of Science and Culture and the Volkswagen Foundation under the program "Zukunft.niedersachsen: Research Cooperation Lower Saxony – Israel" 76251-5615/2023.

Author contributions

Fyodor Morozko and Shadad Watad contributed equally to the conceptualization, methodology, investigation, and formal analysis. Fyodor Morozko developed software. All the authors wrote the original draft of the manuscript. Fyodor Morozko, Shadad Watad, Amir Naser, and Alina Karabchevsky reviewed and edited the manuscript. Alina Karabchevsky supervised the project and acquired funding.

Conflict of interest

The authors declare that they have no competing interests.

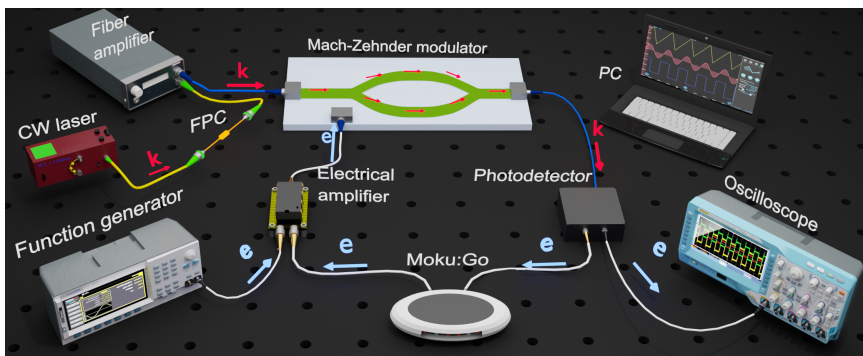
References

- [1] Y. Bengio, *Foundations and Trends® in Machine Learning* **2009**, *2*, 1 1.
- [2] Y. LeCun, Y. Bengio, G. Hinton, *Nature* **2015**, *521*, 7553 436.
- [3] A. N. Tait, M. A. Nahmias, Y. Tian, B. J. Shastri, P. R. Prucnal, In M. Naruse, editor, *Nanophotonic Information Physics*, 183–222. Springer Berlin Heidelberg, Berlin, Heidelberg, ISBN 978-3-642-40223-4 978-3-642-40224-1, **2014**.
- [4] M. Miscuglio, A. Mehrabian, Z. Hu, S. I. Azzam, J. George, A. V. Kildishev, M. Pelton, V. J. Sorger, *Optical Materials Express* **2018**, *8*, 12 3851.
- [5] M. A. Nahmias, T. F. de Lima, A. N. Tait, H.-T. Peng, B. J. Shastri, P. R. Prucnal, *IEEE Journal of Selected Topics in Quantum Electronics* **2020**, *26*, 1 1.
- [6] X. Xu, M. Tan, B. Corcoran, J. Wu, A. Boes, T. G. Nguyen, S. T. Chu, B. E. Little, D. G. Hicks, R. Morandotti, A. Mitchell, D. J. Moss, *Nature* **2021**, *589*, 7840 44.
- [7] J. Feldmann, N. Youngblood, M. Karpov, H. Gehring, X. Li, M. Stappers, M. Le Gallo, X. Fu, A. Lukashchuk, A. S. Raja, J. Liu, C. D. Wright, A. Sebastian, T. J. Kippenberg, W. H. P. Pernice, H. Bhaskaran, *Nature* **2021**, *589*, 7840 52.
- [8] B. J. Shastri, *Nature Photonics* **2021**, *15* 13.
- [9] J. Wu, X. Lin, Y. Guo, J. Liu, L. Fang, S. Jiao, Q. Dai, *Engineering* **2022**, *10* 133.

- [10] A. Hazan, B. Ratzker, D. Zhang, A. Katiyi, M. Sokol, Y. Gogotsi, A. Karabchevsky, *Advanced Materials* **2023**, 2210216.
- [11] Z. Qi, L. Mi, H. Qian, W. Zheng, Y. Guo, Y. Chai, *Advanced Functional Materials* **2023**, 33, 43 2306149.
- [12] H. Jaeger, H. Haas, *Science* **2004**, 304, 5667 78.
- [13] M. Lukoševičius, H. Jaeger, *Computer Science Review* **2009**, 3, 3 127.
- [14] M. Romera, P. Talatchian, S. Tsunegi, F. Abreu Araujo, V. Cros, P. Bortolotti, J. Trastoy, K. Yakushiji, A. Fukushima, H. Kubota, et al., *Nature* **2018**, 563, 7730 230.
- [15] L. Appeltant, M. Soriano, G. Van der Sande, J. Danckaert, S. Massar, J. Dambre, B. Schrauwen, C. Mirasso, I. Fischer, *Nature Communications* **2011**, 2, 1 468.
- [16] T. M. Cover, *IEEE Transactions on Electronic Computers* **1965**, EC-14, 3 326.
- [17] G. V. der Sande, D. Brunner, M. C. Soriano, *Nanophotonics* **2017**, 6, 3 561.
- [18] Y. Paquot, F. Duport, A. Smerieri, J. Dambre, B. Schrauwen, M. Haelterman, S. Massar, *Scientific Reports* **2012**, 2, 1 287.
- [19] L. Larger, M. C. Soriano, D. Brunner, L. Appeltant, J. M. Gutierrez, L. Pesquera, C. R. Mirasso, I. Fischer, *Optics Express* **2012**, 20, 3 3241.
- [20] F. Duport, B. Schneider, A. Smerieri, M. Haelterman, S. Massar, *Optics Express* **2012**, 20, 20 22783.
- [21] R. Martinenghi, S. Rybalko, M. Jacquot, Y. K. Chembo, L. Larger, *Physical Review Letters* **2012**, 108, 24 244101.
- [22] D. Brunner, M. C. Soriano, C. R. Mirasso, I. Fischer, *Nature Communications* **2013**, 4, 1 1364.
- [23] P. Antonik, F. Duport, M. Hermans, A. Smerieri, M. Haelterman, S. Massar, *IEEE Transactions on Neural Networks and Learning Systems* **2017**, 28, 11 2686.
- [24] K. Harkhoe, G. Verschaffelt, A. Katumba, P. Bienstman, G. Van der Sande, *Optics Express* **2020**, 28, 3 3086.
- [25] M. Lukoševičius, In G. Montavon, G. B. Orr, K.-R. Müller, editors, *Neural Networks: Tricks of the Trade: Second Edition*, Lecture Notes in Computer Science, 659–686. Springer, Berlin, Heidelberg, ISBN 978-3-642-35289-8, **2012**.
- [26] X. Hinaut, N. Trouvain, In I. Farkaš, P. Masulli, S. Otte, S. Wermter, editors, *Artificial Neural Networks and Machine Learning – ICANN 2021*, volume 12895, 83–97. Springer International Publishing, Cham, ISBN 978-3-030-86382-1 978-3-030-86383-8, **2021**.
- [27] F. Köster, S. Yanchuk, K. Lüdge, *Journal of Physics: Photonics* **2021**, 3, 2 024011.
- [28] T. Hülser, F. Köster, L. Jaurigue, K. Lüdge, *Optical Materials Express* **2022**, 12, 3 1214.
- [29] N. Trouvain, L. Pedrelli, T. T. Dinh, X. Hinaut, In I. Farkaš, P. Masulli, S. Wermter, editors, *Artificial Neural Networks and Machine Learning – ICANN 2020*, volume 12397, 494–505. Springer International Publishing, Cham, ISBN 978-3-030-61615-1 978-3-030-61616-8, **2020**.
- [30] A. Botchkarev, *Interdisciplinary Journal of Information, Knowledge, and Management* **2019**, 14 045.
- [31] D. Brunner, B. Penkovsky, B. A. Marquez, M. Jacquot, I. Fischer, L. Larger, *Journal of Applied Physics* **2018**, 124, 15 152004.

- [32] A. Rodan, P. Tino, *IEEE Transactions on Neural Networks* **2011**, *22*, 1 131.
- [33] K. Ikeda, *Optics Communications* **1979**, *30*, 2 257.
- [34] K. Ikeda, H. Daido, O. Akimoto, *Physical Review Letters* **1980**, *45*, 9 709.
- [35] A. Neyer, E. Voges, *IEEE Journal of Quantum Electronics* **1982**, *18*, 12 2009.
- [36] T. Erneux, L. Larger, M. W. Lee, J.-P. Goedgebuer, *Physica D: Nonlinear Phenomena* **2004**, *194*, 1-2 49.
- [37] L. Larger, J.-P. Goedgebuer, V. Udaltsov, *Comptes Rendus Physique* **2004**, *5*, 6 669.
- [38] J. Bergstra, R. Bardenet, Y. Bengio, B. Kégl, In *Advances in Neural Information Processing Systems*, volume 24. Curran Associates, Inc., **2011**.
- [39] J. T. Mineichi Kudo, *Japanese Vowels*, **1999**.
- [40] E. Picco, A. Lupo, S. Massar, *IEEE Transactions on Neural Networks and Learning Systems* **2024**, 1–9, conference Name: IEEE Transactions on Neural Networks and Learning Systems.
- [41] U. Paudel, M. Luengo-Kovac, J. Pilawa, T. J. Shaw, G. C. Valley, *Optics Express* **2020**, *28*, 2 1225.
- [42] F. Stelzer, A. Röhm, K. Lüdge, S. Yanchuk, *Neural Networks* **2020**, *124* 158.

Table of Contents



In-situ optimization of multiple parameters of an optoelectronic delay-based reservoir computing system is realized and tested in three benchmark tasks. Accuracy achieved with *in situ* optimization exceeded accuracy obtained with simulation by 17% and 48% in two of the three tasks. Experimental results reveal that the delay timescale is critical for the accuracy of delay-based reservoir computing.

In Situ Optimization of an Optoelectronic Reservoir Computer with Digital Delayed Feedback

1 Dynamics of the optoelectronic oscillator

Figure 1 presents the behavior of the optoelectronic oscillator: Figures (a-c) show cobweb diagrams in stable, periodic, and chaotic regimes, respectively, Figures d-e show simulated and experimentally obtained fixed points in the systems at different settings based on the Ikeda model [3, 1, 2, 5, 4].

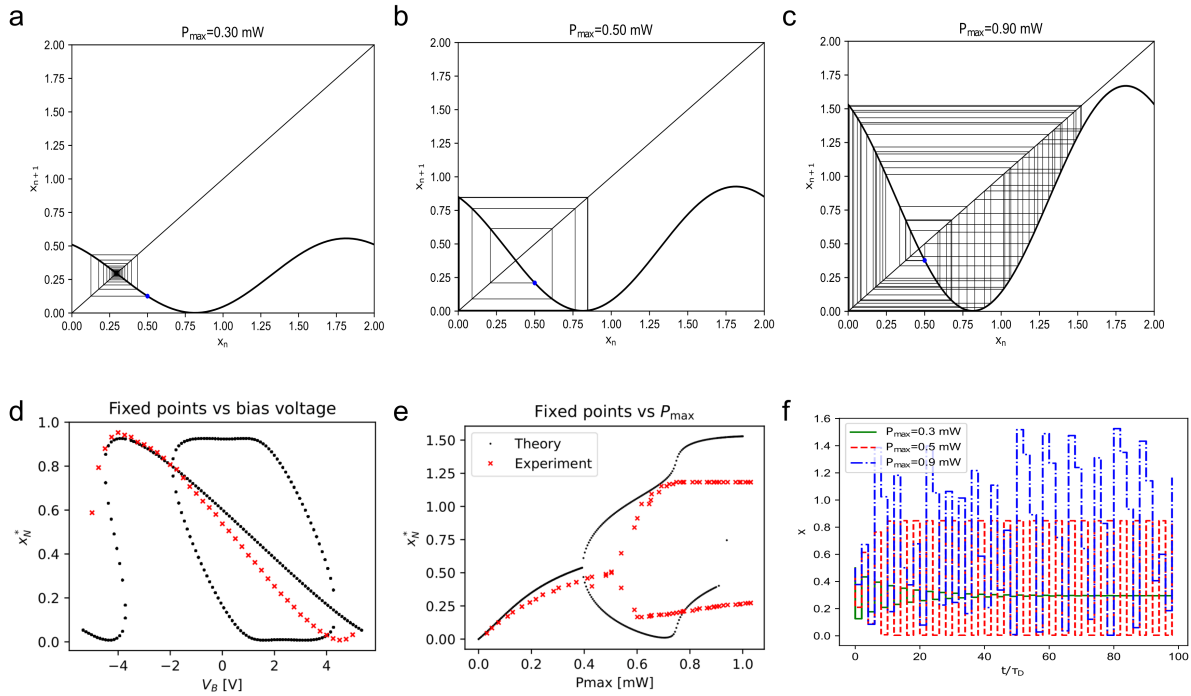


Figure 1: Simulated and experimental results from set-up shown in Figure 2 in the main text: calculated results based on the discrete-time model: (a) stable, (b) periodic, and (c) chaotic regimes. (d-e) Fixed points of the system as a function of (d) bias voltage V_B and (e) optical power P_{\max} , f) Simulated dynamics using discrete-time model

As discussed in [5], if the response time of the system τ is much less than the delay time τ_D $\tau \ll \tau_D$ the continuous-time dynamics of the delayed-feedback system can be efficiently modeled by the discrete-time difference equation

$$x_{n+1} = G/2(1 + M \sin(\pi(x_n + x_b))), \quad (1)$$

where $x_n = V(n\tau_D)/V_\pi$, $x_b = V_B/V_\pi$, and

$$G = P_{\text{out}}G^*/V_\pi \quad (2)$$

is the net gain of the open loop. The graphical solution of the 1 is depicted in **Figure** . The resulting path originates from x_0 in the proximity of x_1 and moves away from x_1 due to instability. However, it is eventually attracted to a stable limit determined by the number of periods. For **Figure 1a**, the period is 1, for **Figure 1b** it is 2, and for **Figure 1c**, the period is 3.

The simulation results of the optoelectronic oscillator are represented in subplots **Figures 1a-c**, which show the cobweb diagrams of the different regimes. The method involves overlapping the cobweb plot with the function $y = x$ to identify the fixed points. **Figure 1a** shows the dynamics of the system in the stable

regime corresponding to the parameters $P_{\max} = 0.3$ mW denotes the maximum power, $V_b = 0$ V represents the bias voltage, $G = 0.56$ signifies the feedback gain, and $M = 0.983$ is defined as the modulation factor. So, in the intersection, we obtain one unstable fixed point. **Figure 1b** shows the periodic regime with $P_{\max} = 0.5$ mW, $V_b = 0$ V and $G = 0.93$. Here, we encounter two unstable fixed points. The chaotic regime is shown in **Figure 1c** with $P_{\max} = 0.9$ mW and $V_b = 0$ V, $G = 1.49$. By examining the three subplots, we can observe that the stability of x_{n+1} vs. x_n is decreasing compared to the stable regime in **Figure 1a**. Hopf bifurcations are shown in **Figures 1d-f**. Where **Figure 1d** demonstrates the equilibrium values of the first iteration "N=1" for the "Number of the equation" considering the bias voltage. The black curve represents the simulated results, while the red curve represents the experimental measurements, considering the parameters $G = 0.93$ and $M = 0.983$. The graph showcases stable regions with a single stable solution denoting system stability. In contrast, the bistable and periodic regions exhibit three solutions: two stable and one unstable. The presence of periodic solutions arises from the equation's bifurcation of stable states. Simulated results are used to validate the theoretical predictions, ensuring the accuracy and reliability of the findings. **Figures 1e** which exhibits a cascade of periodic solutions with fixed parameters $G = 0.93$ and $M = 0.983$. The graph presents a depiction of the stable and unstable fixed points as a function of the maximum power, P_{\max} , up to iteration $N = 8$. A significant observation is that as P_{\max} increases, so does the net feedback gain, G , leading to a growing number of bifurcations. Notably, this cascade of periodic solutions appears to extend infinitely until reaching the critical value $G_c = 1.49$. Upon reaching it, the system transforms into an aperiodic(chaotic) regime, resulting in the absence of periodic solutions. **Figure 1f** depicts stable, periodic, and chaotic regimes in the time domain.

2 Electro-optic modulator driver

To drive the electro-optical modulator which has $50\ \Omega$ characteristic impedance the low-current output signal of the Moku:Go's FIR filter needed to be amplified. For this purpose we have built a driver circuit based on a high-speed analog operational amplifier (LM7171, Texas Instruments) as shown in Figure 2. We have incorporated a voltage divider at the input of the amplifier to adjust the relative strengths of the delayed feedback and input signal.

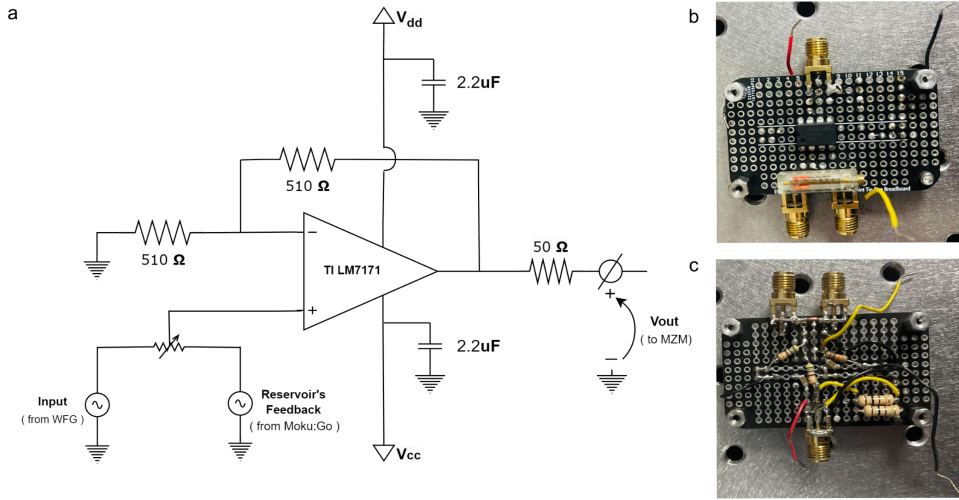


Figure 2: (a) Schematic of the electro-optic modulator driver. (b-c) design of the amplifier board.

References

- [1] K. Ikeda, H. Daido, and O. Akimoto. Optical Turbulence: Chaotic Behavior of Transmitted Light from a Ring Cavity. *Physical Review Letters*, 45(9):709–712, September 1980.
- [2] K. Ikeda, K. Kondo, and O. Akimoto. Successive Higher-Harmonic Bifurcations in Systems with Delayed Feedback. *Physical Review Letters*, 49(20):1467–1470, November 1982.
- [3] Kensuke Ikeda. Multiple-valued stationary state and its instability of the transmitted light by a ring cavity system. *Optics Communications*, 30(2):257–261, August 1979.

- [4] Laurent Larger, Jean-Pierre Goedgebuer, and Vladimir Udaltsov. Ikeda-based nonlinear delayed dynamics for application to secure optical transmission systems using chaos. *Comptes Rendus Physique*, 5(6):669–681, July 2004.
- [5] A. Neyer and E. Voges. Dynamics of electrooptic bistable devices with delayed feedback. *IEEE Journal of Quantum Electronics*, 18(12):2009–2015, December 1982.